Supplementary information

Low-coordinate Cu_1–N_2 sites in single-atom catalyst for highly efficient propylene epoxidation with molecular oxygen

Yueming Qiu[1], Yichen Zhang[1], Siqiang Xiao[1], Jian Tian[1], Ronghui Zhang[1], Luying Sun[2], Kok Bing Tan[1], Gang Fu[1,2,*], Yih-Shing Duh[1,3], Qingbiao Li[1,4,*], and Jiale Huang[1,3,*]

[1]Department of Chemical and Biochemical Engineering, College of Chemistry and Chemical Engineering, Xiamen University, 422 Siming South Road, Xiamen, Fujian 361005, P. R. China

[2]State Key Laboratory of Physical Chemistry of Solid Surfaces, College of Chemistry and Chemical Engineering, Xiamen University, 422 Siming South Road, Xiamen, Fujian 361005, P. R. China

[3]Reactive Hazards Evaluation Laboratory, Gulei Innovation Institute, Xiamen University, Zhangzhou, Fujian 363105, P. R. China

[4]College of Ocean Food and Biology Engineering, Jimei University, Xiamen, Fujian 361021, P. R. China

E-mail: gfu@xmu.edu.cn (Gang Fu), kelqb@xmu.edu.cn (Qingbiao Li), cola@xmu.edu.cn (Jiale Huang)

This file includes:

Supplementary Experimental and Theoretical Procedures

Chemicals. Copper chloride ($CuCl_2$, ≥99.9%) and melamine were purchased from Macklin Reagent company. L-cysteine (≥99%) and ethanol (AR) were purchased from Sinopharm Chemical Reagent Co., Ltd. All chemical reagents were used as received without further purification. All aqueous solutions were prepared using deionized water with a resistivity of 18.2 MΩ cm^{-1}.

Synthesis of Cu_{NP}/C_3N_4–L. For the synthesis of Cu_{NP}/C_3N_4–L, 0.3 g C_3N_4–L was transferred to the metal aqueous solution (0.04 M) and then was stirred for 30 min at room temperature. After that, 0.5 M $NaBH_4$ was injected dropwise into the solution and the mixed solution was adequately stirred. Finally, the dark precipitate was centrifuged and was rinsed with deionized water before being dried under vacuum at 50 °C overnight.

Characterizations. X-ray diffraction (XRD) patterns were examined by an X'Pert-Pro X-ray powder diffractometer equipped with a Cu radiation source (wavelength: 0.15406 nm) with the operation voltage and operation current being 50 mA and 40 kV, respectively. X-ray photoelectron spectroscopy (XPS) was conducted on a diffractometer (Thermo Scientific K-Alpha) using Al Kα (1486.6 eV) radiation. The likely charging of the sample was corrected by calibrating the binding energy (B.E.) of the adventitious carbon (C 1*s*) to 284.8 eV. The quantitative measurement of the Cu content in all samples was performed using the inductively coupled plasma optical emission spectrometry (ICP-OES, Agilent, 5100 SVDV) characterization method. $^{13}C/^{1}H$ cross polarization-magic angle spinning (CP-MAS) NMR was obtained via a

Bruker 400MHz Avance III spectrometer equipped with a 4 mm standard bore CP MAS probe head. The Brunauer-Emmett-Teller surface area and Barrett-Joyner-Halenda (BJH) porosity of samples were analyzed by the N_2 adsorption/desorption isotherms by using Micromeritics (ASAP 2460) at -196 °C, then dried at 100 °C for 6 h under vacuum conditions. Renishaw inVia spectrometer was used to record Raman in the region of 200-800 nm, using a 532 nm laser as the source. Diffuse reflectance infrared Fourier transform spectroscopy (DRIFTS) was measured on a Nicolet 6700 FT-IR spectrometer equipped with an *in situ* Fourier transform infrared reaction cell and a liquid nitrogen cooled mercury-cadmium-telluride detector. 50.0 mg sample (mixture of catalyst and KBr) was loaded on the sample stage of the reaction cell, that is to be tested, and the sample was purged and evacuated with nitrogen for 1 h before the adsorption experiments, whose spectrum was taken as the background spectra. Next, probe molecule would be admitted into the reaction cell and the DRIFTS spectrum was recorded after the chemisorption. Electrochemical impedance spectroscopy (EIS) measurements were based on a Biologic VMP3 electrochemical workstation. Atomic force microscopy (AFM) was conducted on a Bruker Dimension. Scanning electron microscopy (SEM) was performed on a Zeiss Sigma electron microscope to characterize the morphology of all samples. Transmission electron microscopy (TEM) was performed on a FEI/Philips TECNAI-F30 transmission electron microscope at an acceleration voltage of 300 kV. High-angle annular dark-field STEM energy dispersive X-ray spectroscopy (HAADF-STEM-EDS) was collected on Thermalfisher scientific titan themsis Z scanning transmission electron microscope with double Cs correctors at

an acceleration voltage of 300 kV.

X-ray absorption spectroscopy (XAS) and simulations. Quick-scanning X-ray absorption spectroscopy beamline using bending magnet at Singapore Synchrotron Light Source (SSLS), including X-ray absorption near-edge structure (XANES) and extended X-ray absorption fine structure (EXAFS) spectra at the Cu K-edge, and the Athena (version 0.9.26) was used to analyze the data. The EXAFS fittings were conducted with the Artemis (version 0.9.26). The EXAFS of Cu foil was fitted and the obtained amplitude reduction factor value ($S_0^2 = 0.88$) was set in the EXAFS analysis. Based on the above results, the coordination numbers in the Cu–N scattering path of catalysts were found out. EXAFS fitting of catalyst was conducted through a least-squares fitting in R space for the k^3-weighted Fourier transformed data using Artemis, which follows the model structure of $Cu_1–N_2$, $Cu_1–N_3$ and $Cu_1–N_4$ SACs (**Supplementary Fig. 10**) used for DFT calculations.

Catalytic performance evaluation. The propylene oxidation with molecular oxygen was performed in a continuous flow fixed-bed microreactor with an axial quartz sheathed thermocouple under atmospheric pressure. 50.0 mg catalyst sample was equipped in a quartz reactor. The reactant gas mixture (O_2: C_3H_6: N_2 = 5: 10: 85 vol.%) with a flow rate of 30 mL min^{-1} was introduced into the reactor to start the reaction and the reaction temperature was increased from 200 °C to 350 °C at a rate of 3 °C min^{-1}. In order to prevent condensation of the products, the lines and valves of the reactor and the gas chromatographs were heated to 110 °C. The reactants and product were analyzed via two gas chromatographs (GC) equipped with three columns in real time.

The outlet CO_2, C_3H_6, and O_2 were analyzed by a thermal conductivity detector (TCD, separated by a Porapak column and a molecular sieve 5A column). The outlet propylene oxide (PO), acrolein, acetone, propionaldehyde, isopropanol and acetaldehyde products were detected by a flame ionization detector (FID, separated by a capillary column). Considering the difference of carbon number in each product, the catalytic activity and selectivity of propylene oxidation were calculated as the following equations:

$$X_i = R_i \times A_i \tag{1}$$

$$\sum X_i = \sum X_{Products,C3} + \sum \frac{2 \times X_{Products,C2}}{3} + \sum \frac{X_{Products,C1}}{3} \tag{2}$$

$$C_{C3H6} = \sum \frac{X_i}{X_{C3H6,infeed}} \times 100\% \tag{3}$$

$$S_i = \frac{N_i}{3} \times \frac{X_i}{\sum X_i} \times 100\% \tag{4}$$

The formation rate of PO was calculated as follows:

$$\text{PO formation rate} = \frac{C_{C3H6} \times F_{C3H6} \times Pressure \times S_{PO}}{R \times T \times m_{cat}} \times 100\% \tag{5}$$

Where X_i represents the concentration of reactants or products, A_i represents conversion of the peak area obtained by GC, R_i is the relative correction factor resulting from the standard gases, C_{C3H6} represents C_3H_6 conversion, $X_{C3H6,infeed}$ represents the concentrations of C_3H_6 at the inlet, N_i represents the carbon number in each product, S_i represents the selectivity of various products. F_{C3H6} represents the flow rate of C_3H_6, m_{cat} represents the mass of catalyst.

Computational details. The Vienna ab initio simulation package (VASP 5.3.3) was used for all periodic density functional theory (DFT) simulations[1,2]. The Perdew-Burke-Ernzerhof (PBE) generalized gradient approximation was used to handle exchange and correlation (GGA)[3]. The valence electrons were defined by cutoff energy of 400 eV,

and the core electrons were substituted by pseudo-potentials from the projector augmented wave (PAW)[4,5]. The Monkhorst-Pak approach was used to create K-points sampling for all structural models with a 3×3×1 mesh[6]. The Hellman-Feynman forces on each ion were reduced to less than 0.02 eV/A by relaxing all internal structural parameters. The minimal energy reaction pathways were calculated using the Climbing Image Nudged Elastic Band technique (CI-NEB)[7]. Using the quasi-Newton technique, the final transition state structures were improved until the Hellman-Feynman forces on each ion were less than 0.05 eV/A.

The free energy of the reaction is calculated by the following equation:

$$\Delta G = \Delta E + \Delta ZPE - T\Delta S \quad (6)$$

Where G, E, ZPE, T, and S in the equation represent Gibbs free energy, total energy, zero-point energy, temperature, and entropy respectively. The zero-point energies (ZPE) were subsequently determined based on the harmonic frequencies.

Supplementary Figures

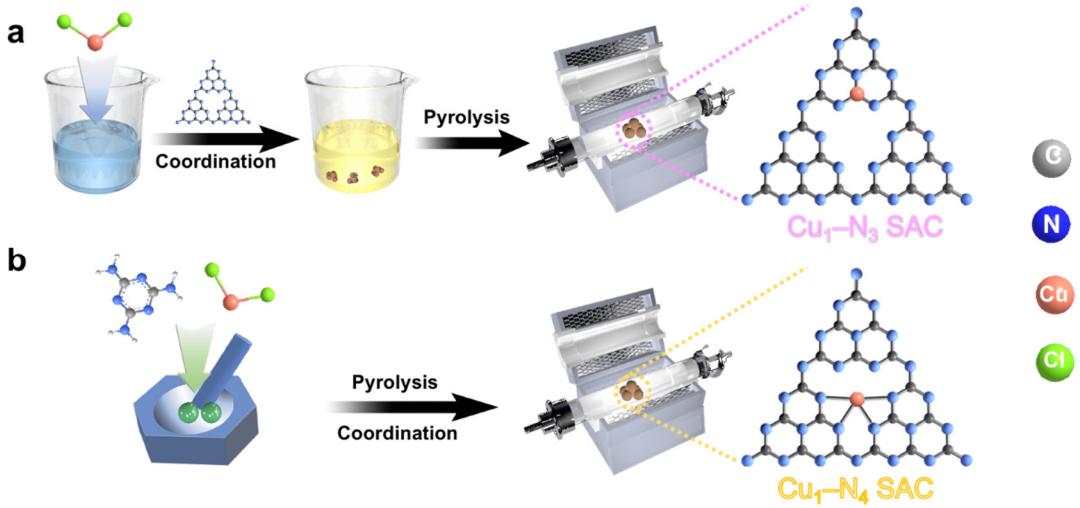

Supplementary Figure 1 | Schematic illustration. Scheme for the synthesis of (**a**) Cu_1–N_3 and (**b**) Cu_1–N_4 SACs.

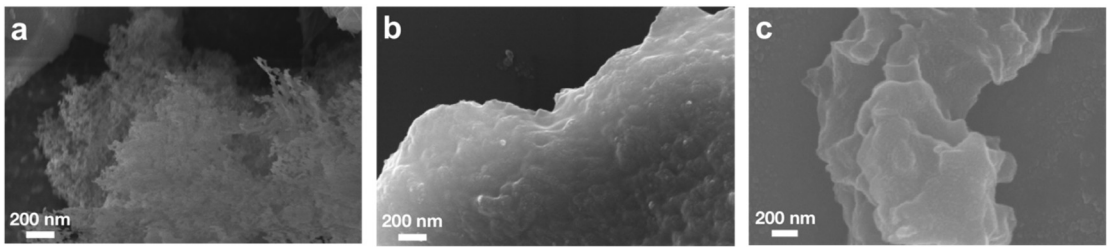

Supplementary Figure 2 | Characterizations of various catalysts. SEM images of (**a**) Cu_1–N_2 (**b**) Cu_1–N_3 and (**c**) Cu_1–N_4 SACs.

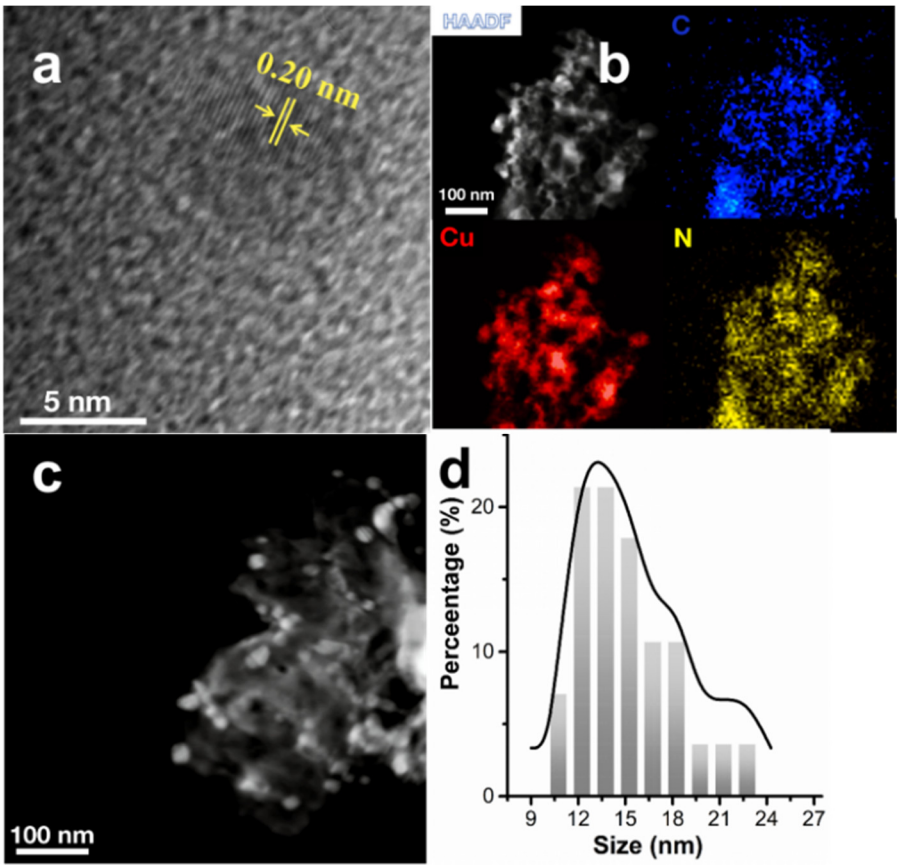

Supplementary Figure 3 | Microscopic characterizations. (**a**) TEM image of Cu_{NP}/C_3N_4–L. (**b**) Element mapping images of Cu_{NP}/C_3N_4–L. (**c**) Aberration-corrected HAADF-STEM image of Cu_{NP}/C_3N_4–L. (**d**) Size distribution of Cu_{NP}/C_3N_4–L.

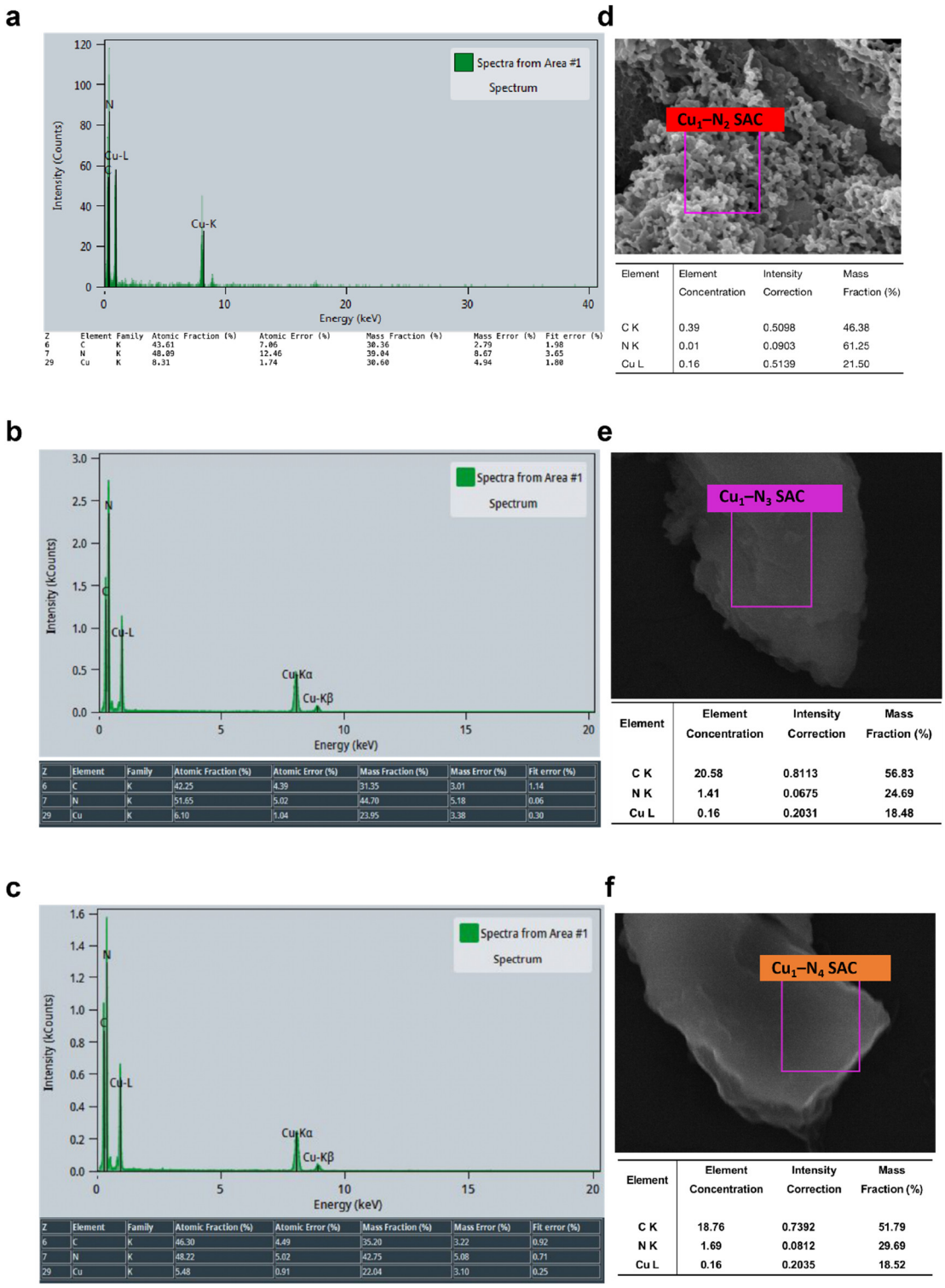

Supplementary Figure 4 | Characterizations of Cu SACs. Selected-area energy dispersive X-ray spectroscopy of (**a**) Cu_1–N_2 (**b**) Cu_1–N_3 and (**c**) Cu_1–N_4 SACs from aberration-corrected HAADF-STEM. Selected-area energy dispersive X-ray spectroscopy of (**d**) Cu_1–N_2 (**e**) Cu_1–N_3 and (**f**) Cu_1–N_4 SACs from SEM.

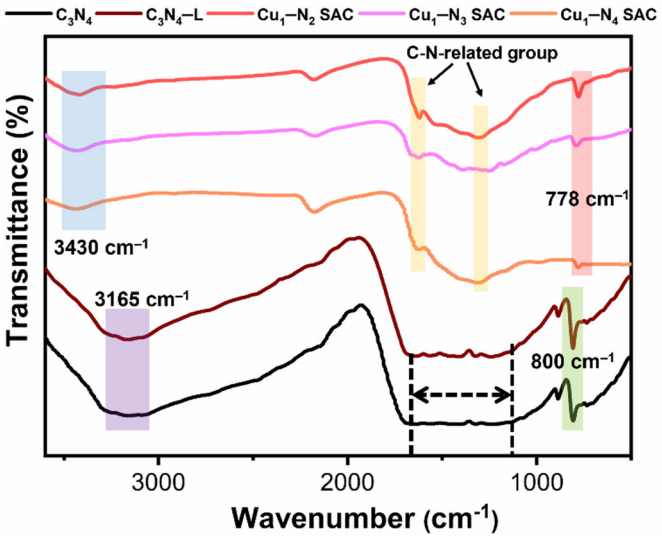

Supplementary Figure 5 | Characterizations of various catalysts. FT-IR spectra of C_3N_4, C_3N_4–L, Cu_1–N_2, Cu_1–N_3 and Cu_1–N_4 SACs.

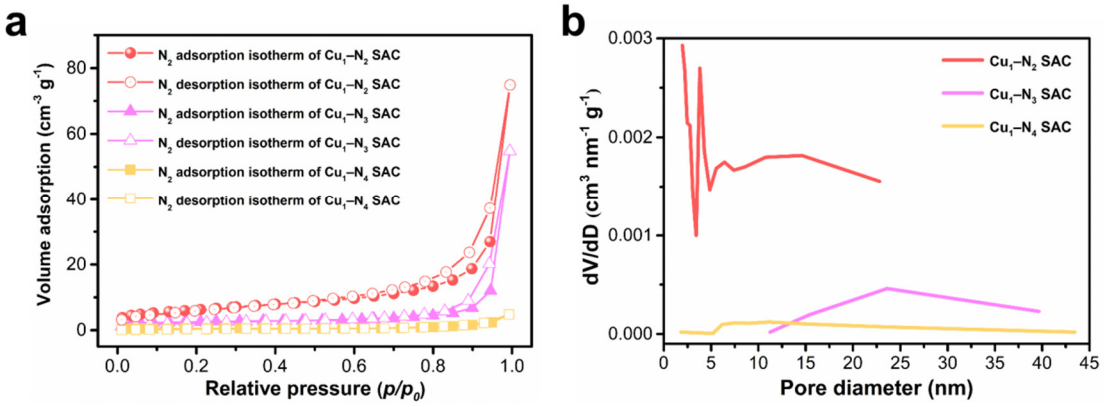

Supplementary Fig. 6 | Physicochemical properties of carriers. (a) N_2 adsorption/desorption isotherms and **(b)** pore size analysis of C_3N_4–L, Cu_1–N_2, Cu_1–N_3 and Cu_1–N_4 SACs.

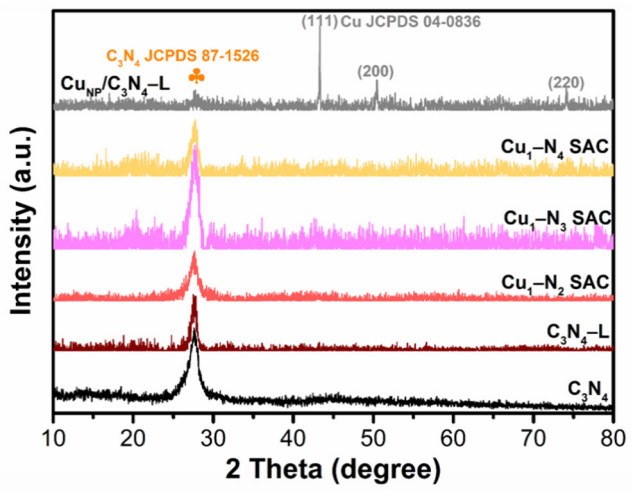

Supplementary Figure 7 | Characterizations of various catalysts. XRD pattern of C_3N_4, C_3N_4–L, Cu_1–N_2 SAC, Cu_1–N_3 SAC, Cu_1–N_4 SAC and Cu_{NP}/C_3N_4–L.

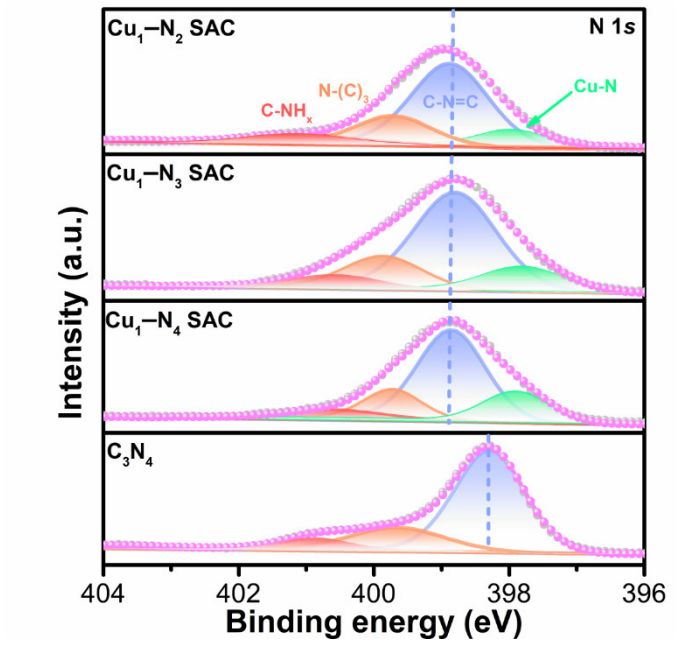

Supplementary Fig. 8 | XPS spectra of various catalysts. N 1*s* XPS spectra of C_3N_4, Cu_1–N_2, Cu_1–N_3 and Cu_1–N_4 SACs.

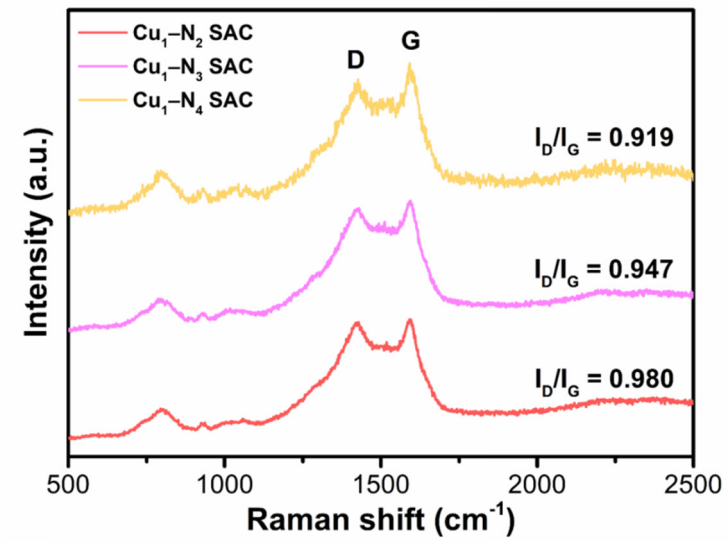

Supplementary Figure 9 | Characterizations of various catalysts. Raman pattern of Cu_1–N_2, Cu_1–N_3 and Cu_1–N_4 SACs.

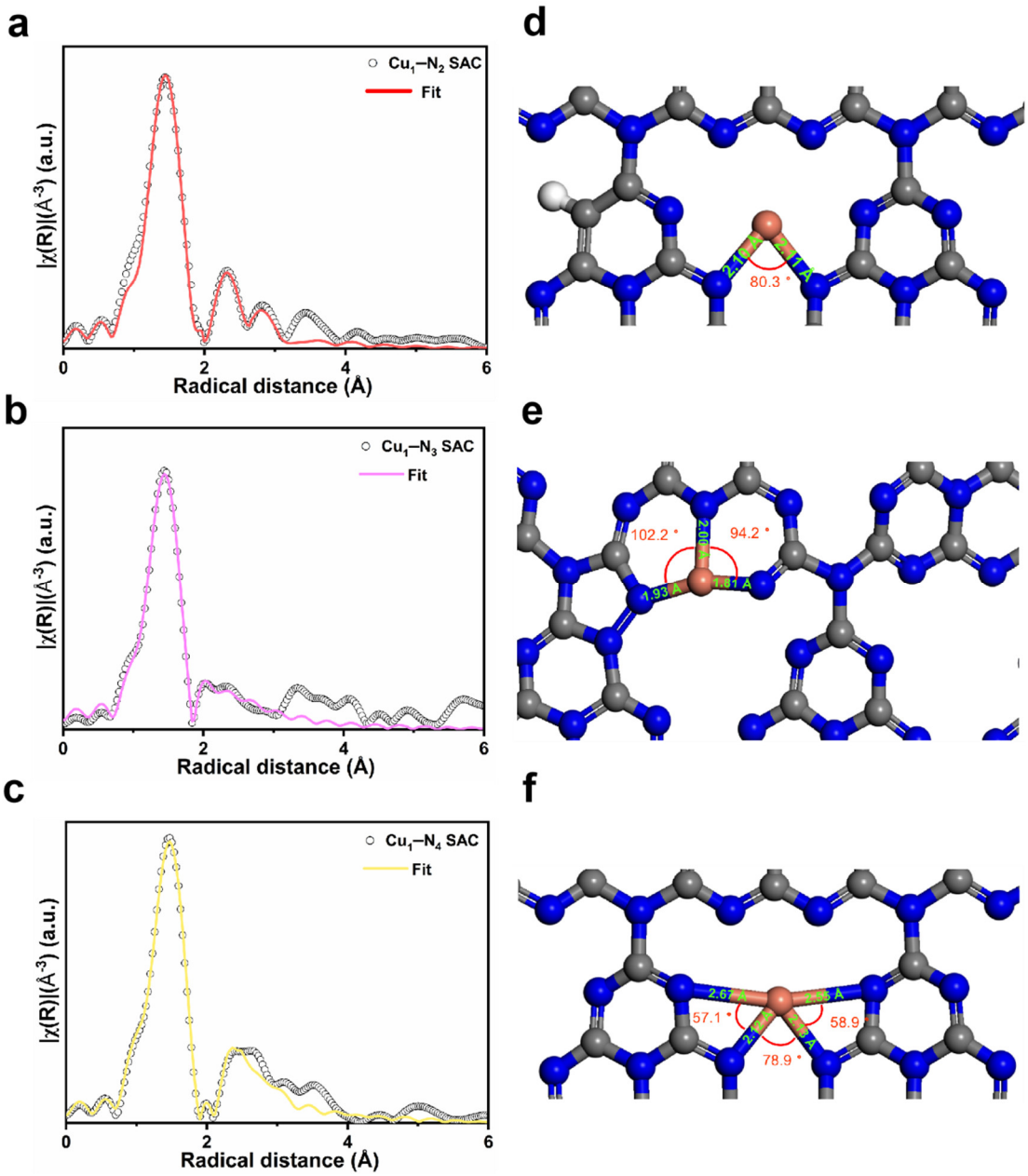

Supplementary Figure 10 | The corresponding fitting results and atomic configurations. (a) The corresponding EXAFS fitting results of (**a**) Cu_1–N_2 (**b**) Cu_1–N_3 and (**c**) Cu_1–N_4 SACs. Computational models for (**d**) Cu_1–N_2 (**e**) Cu_1–N_3 and (**f**) Cu_1–N_4 SACs. Orange: Cu atoms, blue: N atoms, grey: C atoms and white: H atoms.

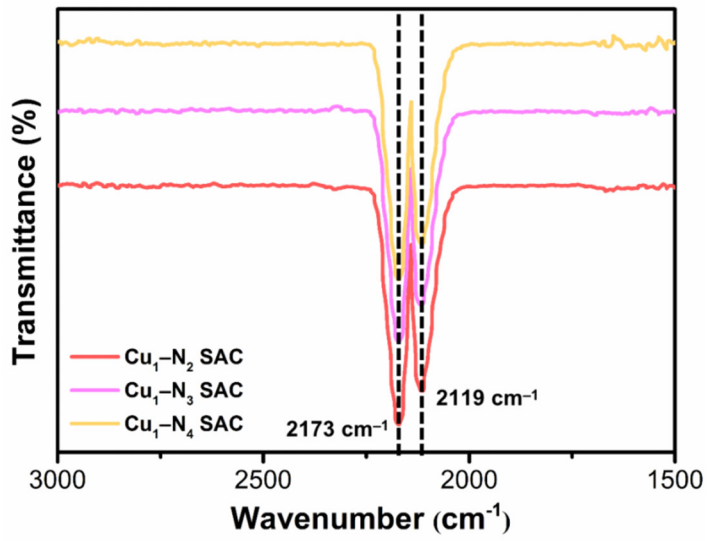

Supplementary Figure 11 | Characterizations of various catalysts. *In situ* DRIFTS of CO adsorption of Cu_1–N_2, Cu_1–N_3 and Cu_1–N_4 SACs.

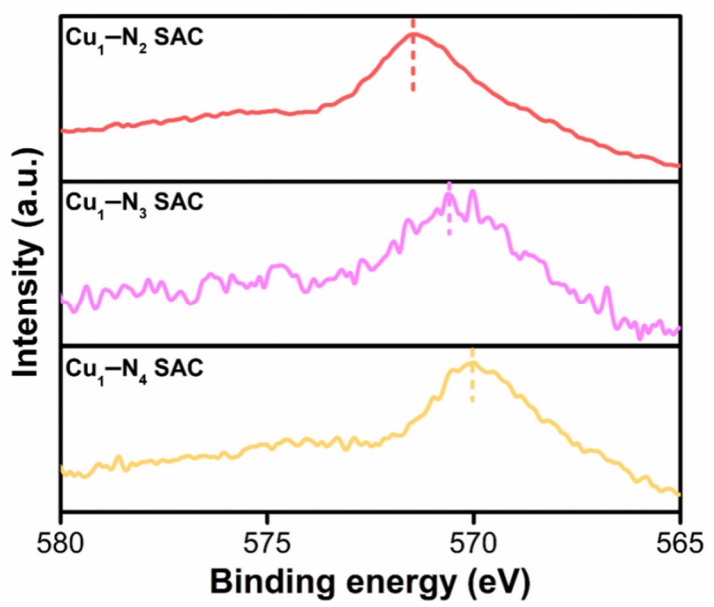

Supplementary Figure 12 | Structural analysis of various catalysts. Cu LMM spectra of Cu_1–N_2, Cu_1–N_3 and Cu_1–N_4 SACs.

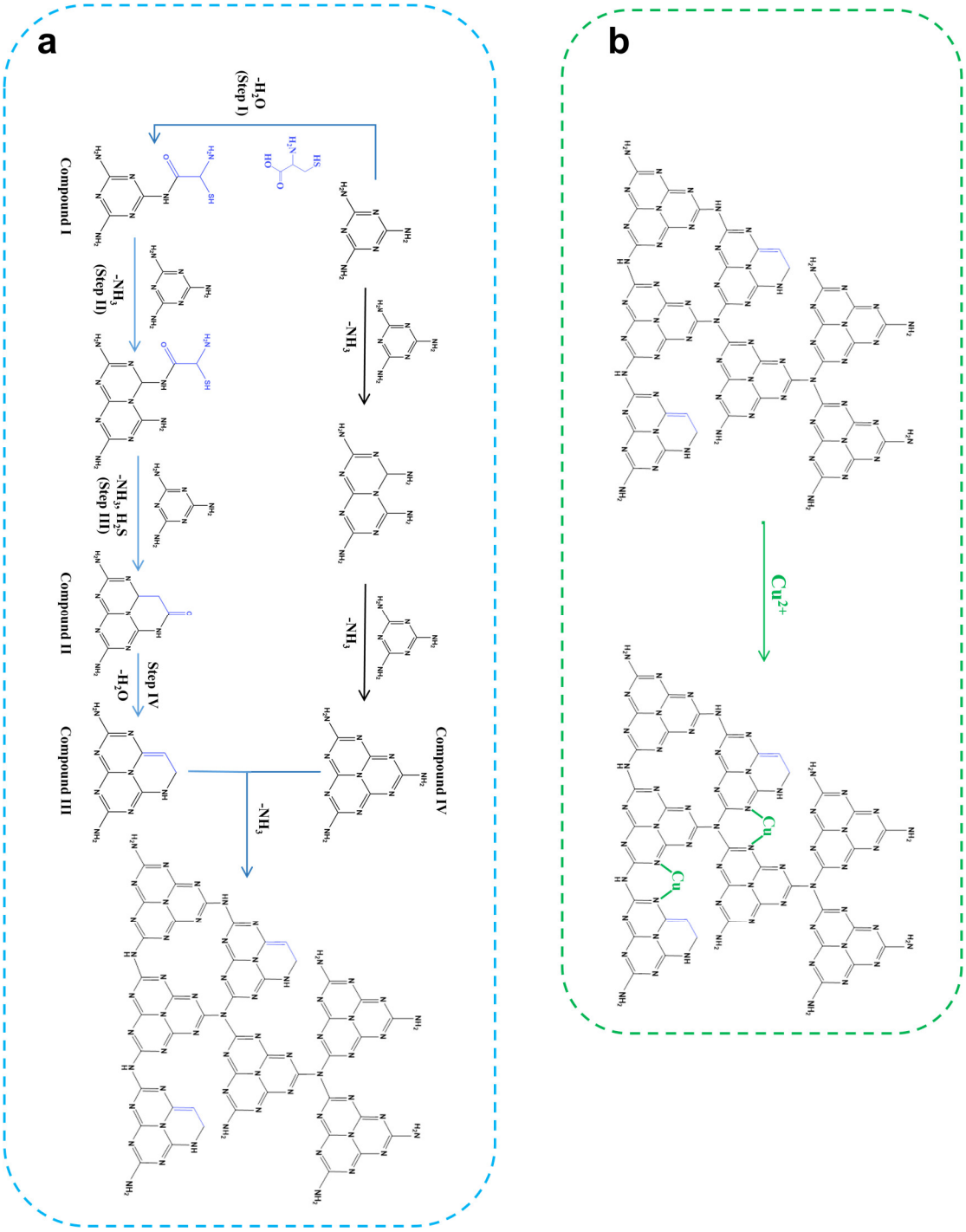

Supplementary Figure 13 | Schematic illustration. (a) Schematic illustration of the synthesis route of C_3N_4–L. **(b)** A plausible formation mechanism of low-coordinated Cu_1–N_2 centres.

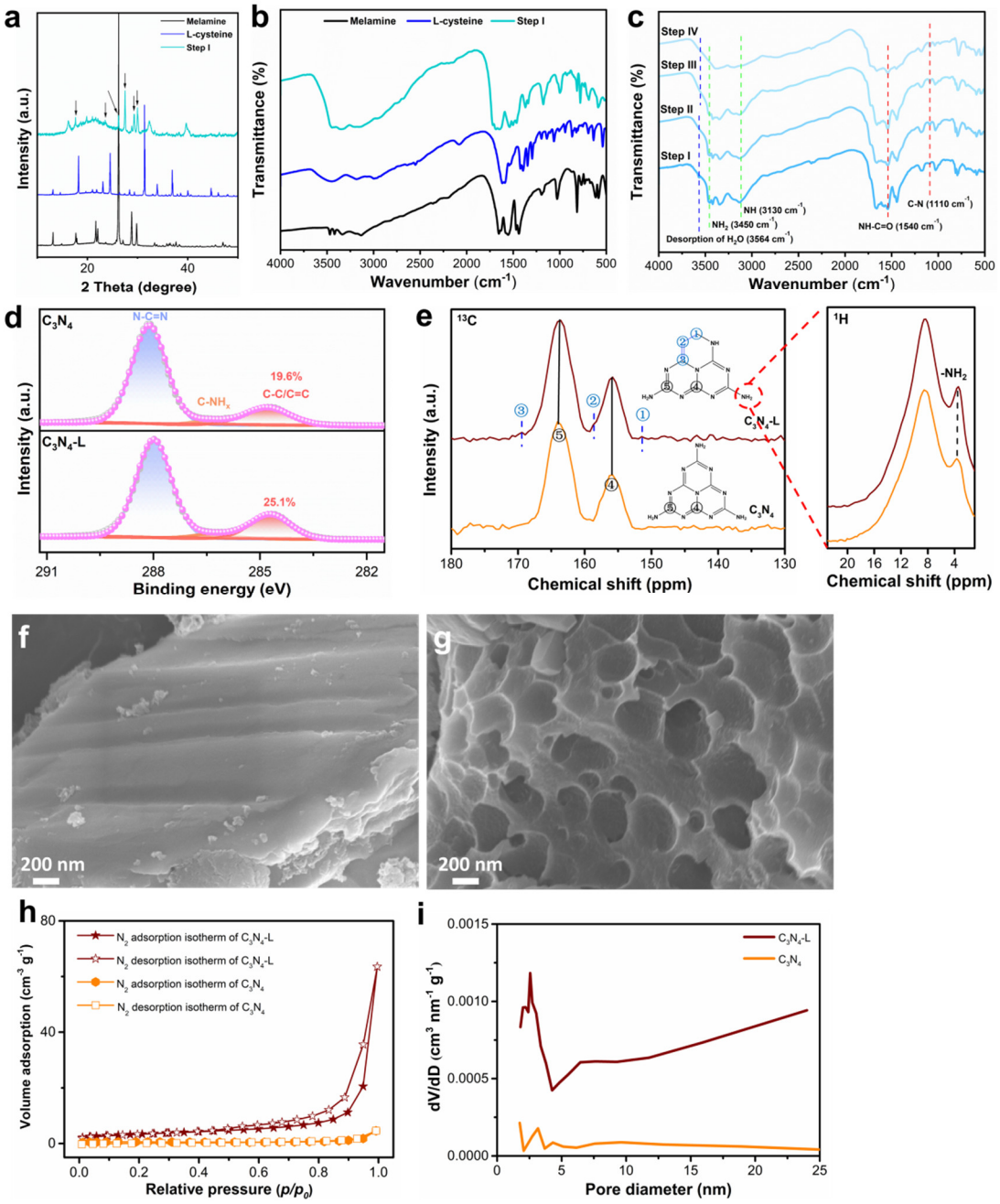

Supplementary Figure 14 | Characterizations and physicochemical properties of carriers. (a) XRD pattern and **(b)** FT-IR spectra of melamine, L-cysteine and precursor. **(c)** FT-IR spectra of precursor in different steps. **(d)** C 1*s* XPS spectra of C_3N_4 and C_3N_4–L. **(e)** $^{13}C/^{1}H$ CP-MAS NMR spectra of C_3N_4 and C_3N_4–L. SEM images of **(f)** C_3N_4 and **(g)** C_3N_4–L. **(h)** N_2 adsorption/desorption isotherms and **(i)** pore size analysis of pristine C_3N_4 and C_3N_4–L.

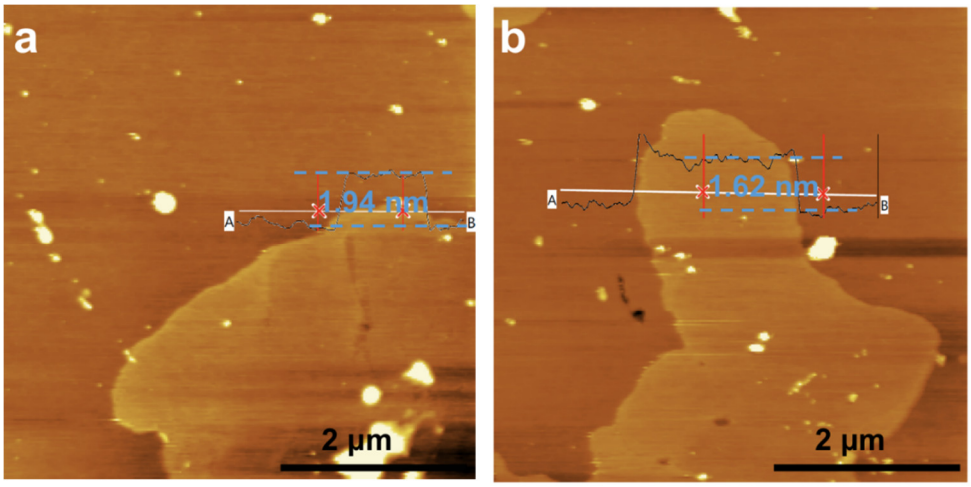

Supplementary Figure 15 | hickness measurements of samples. AFM images and height profiles of **(a)** C_3N_4–L, **(b)** Cu_1–N_2 SAC.

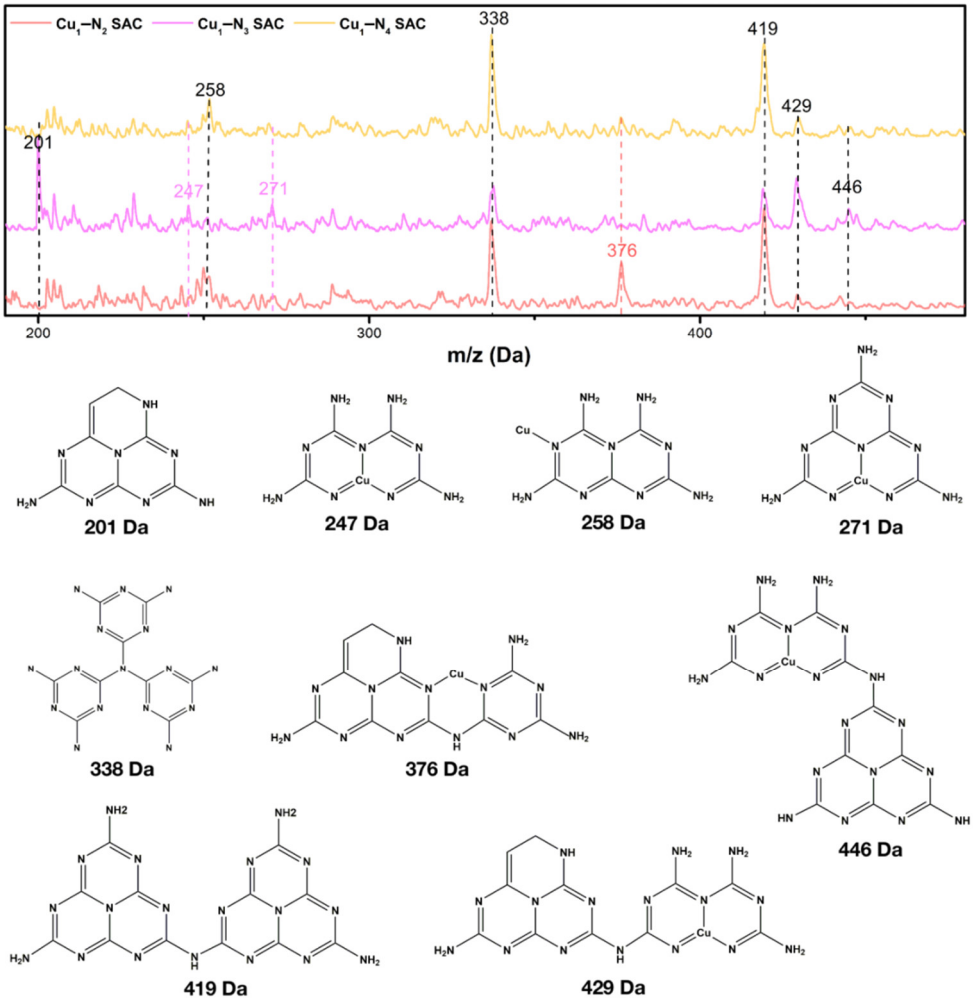

Supplementary Figure 16 | Characterizations of Cu SAC. MALDI-TOF MS spectra of Cu_1–N_2, Cu_1–N_3 and Cu_1–N_4 SACs.

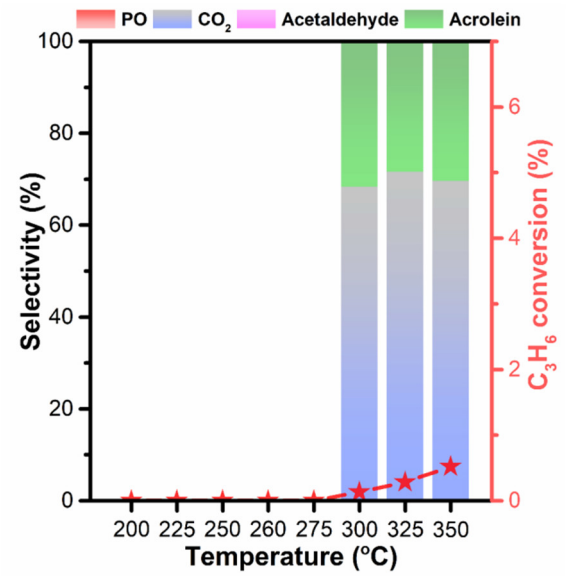

Supplementary Figure 17 | Catalytic performance of propylene epoxidation with O_2. Product selectivity and C_3H_6 conversion at different reaction temperatures over pristine carbon nitride without metal loading. Reaction conditions: C_3H_6: O_2: N_2 = 10: 5: 85 vol.%, GHSV = 36,000 h^{-1}, 50.0 mg catalyst.

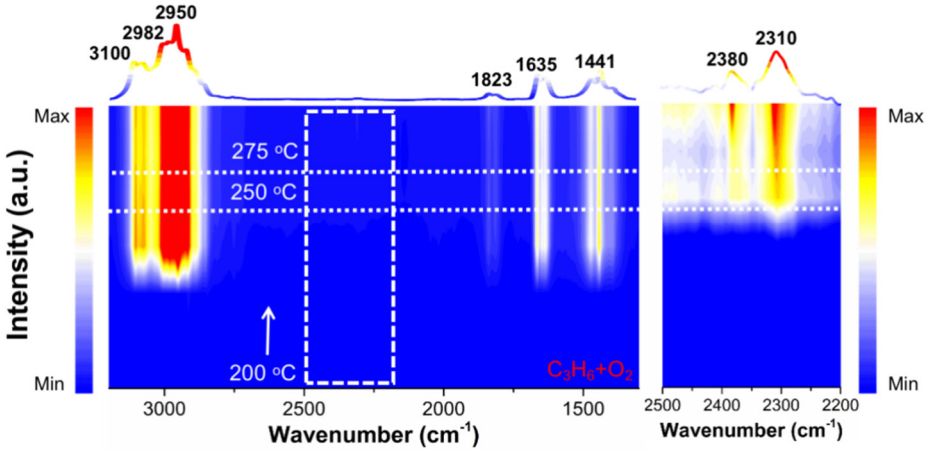

Supplementary Figure 18 | *In situ* DRIFTS spectra of propylene epoxidation with O_2 at different temperatures. The collected DRIFT spectra after exposing Cu_1–N_2 SAC to the mix flow of C_3H_6, O_2 and N_2 (10: 5: 85 vol.%).

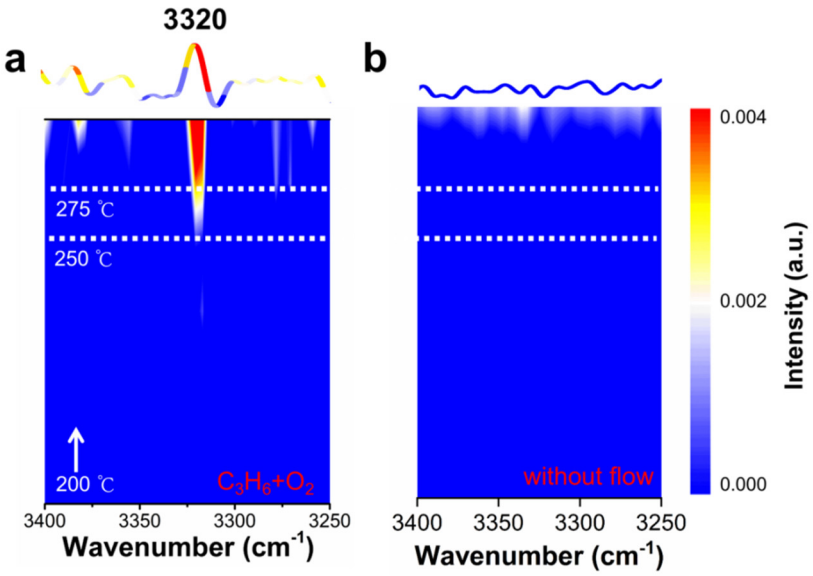

Supplementary Figure 19 | *In situ* DRIFTS spectra of propylene epoxidation with O_2 at different temperatures. The collected DRIFT spectra **(a)** after exposing Cu_1–N_2 SAC to the mix flow of C_3H_6, O_2 and N_2 (10: 5: 85 vol.%) and **(b)** without flow.

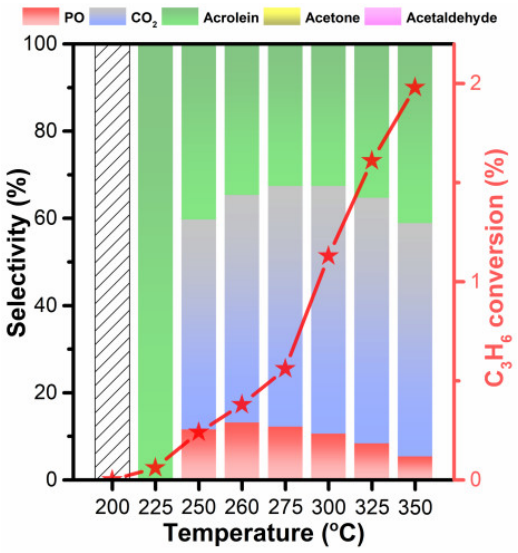

Supplementary Figure 20 | Catalytic performance of propylene epoxidation with O_2. Product selectivity and C_3H_6 conversion at different reaction temperatures over Cu_{NP}/C_3N_4–L. Reaction conditions: C_3H_6: O_2: N_2 = 10: 5: 85 vol.%, GHSV = 36,000 h^{-1}, 50.0 mg catalyst.

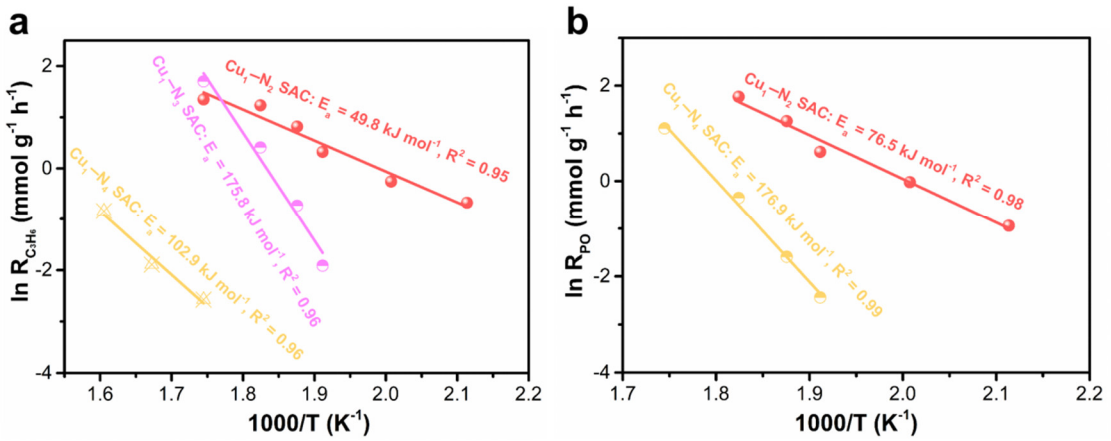

Supplementary Figure 21 | Catalytic performance of propylene epoxidation with O_2. Arrhenius plots of propylene epoxidation catalyzed over Cu_1–N_2, Cu_1–N_3 and Cu_1–N_4 SACs for **(a)** C_3H_6 reaction rates and **(b)** PO formation rates.

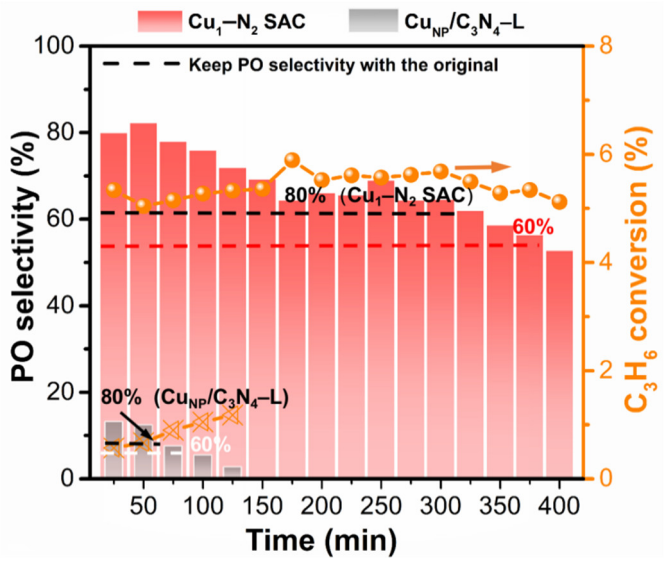

Supplementary Figure 22 | Catalytic performance of propylene epoxidation with O_2. Stability test over Cu_1–N_2 SAC and Cu_{NP}/C_3N_4–L. Reaction conditions: C_3H_6: O_2: N_2 = 10: 5: 85 vol.%, T = 275 °C, GHSV = 36,000 h^{-1}, 50.0 mg catalyst.

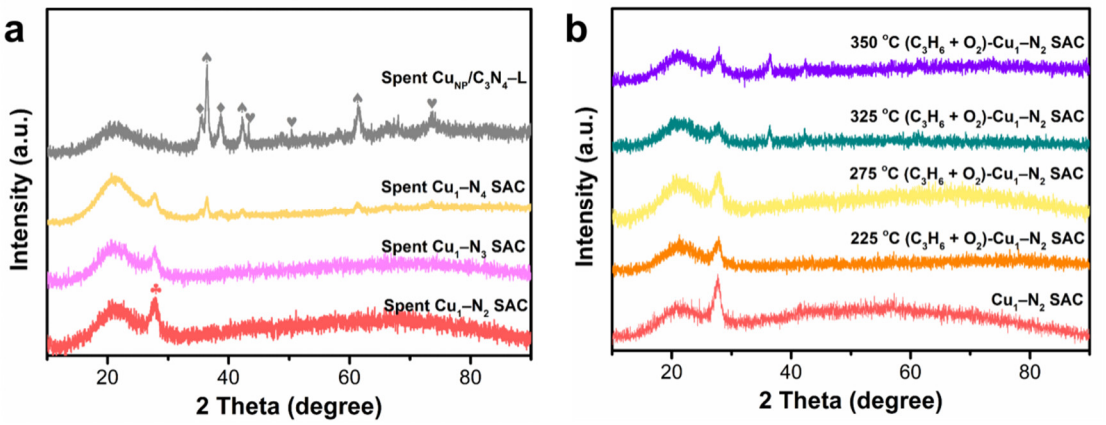

Supplementary Figure 23 | XRD patterns of spent catalysts. The XRD patterns of **(a)** spent Cu_1–N_2 SAC, Cu_1–N_3 SAC, Cu_1–N_4 SAC and Cu_{NP}/C_3N_4–L, and **(b)** spent Cu_1–N_2 SAC at the mixture of C_3H_6, O_2 and N_2 (10: 5: 85 vol.%) with different temperatures. "♣, ♥, ♠, ♦" represent the characteristic peaks of C_3N_4, Cu, Cu_2O and CuO, respectively.

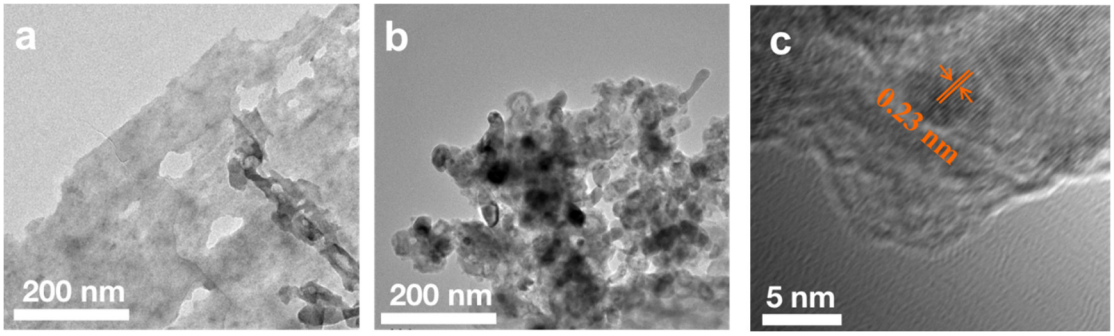

Supplementary Figure 24 | Characterizations of spent catalysts. TEM images of **(a)** spent Cu_1–N_2 SAC and **(b)** spent Cu_{NP}/C_3N_4–L. **(c)** HRTEM image showing the lattice fringes of CuO (111) in spent Cu_{NP}/C_3N_4–L.

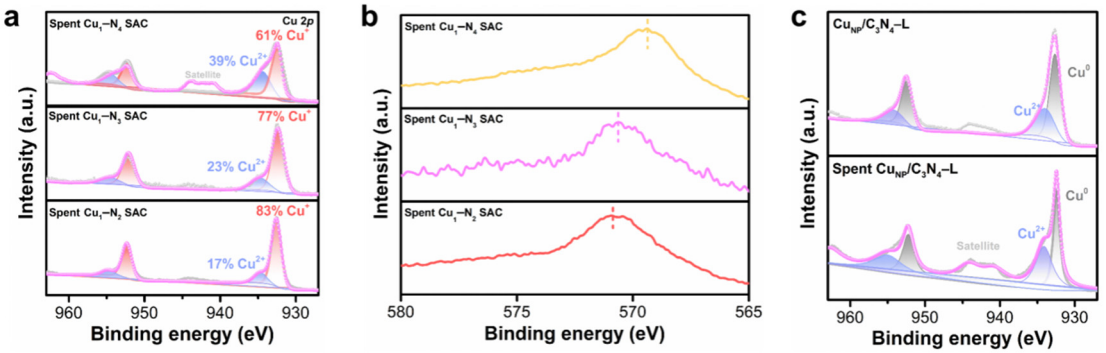

Supplementary Figure 25 | Characterizations of spent catalysts. (a) Cu 2*p* XPS spectra and **(b)** Cu LMM spectra of spent Cu_1–N_2, Cu_1–N_3 and Cu_1–N_4 SACs. **(c)** Cu 2*p* XPS spectra of Cu_{NP}/C_3N_4–L and spent Cu_{NP}/C_3N_4–L.

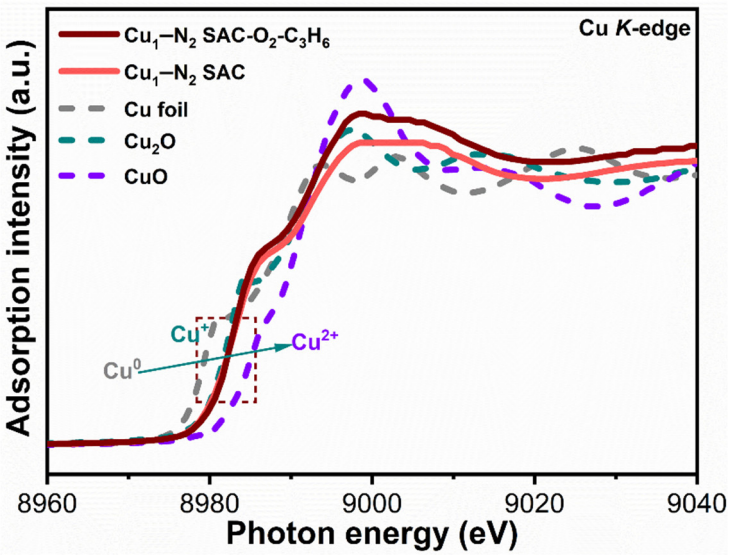

Supplementary Figure 26 | Structural characterizations. Cu *K*-edge XANES of Cu foil, Cu_2O, CuO, Cu_1–N_2 SAC and Cu_1–N_2 SAC-O_2-C_3H_6.

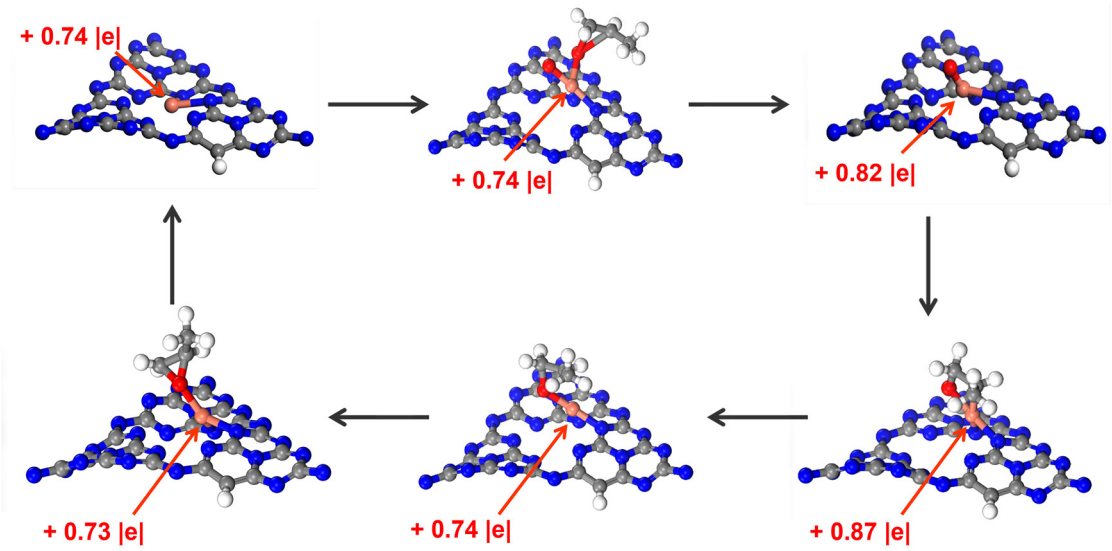

Supplementary Figure 27 | DFT analysis. Dynamic change of Bader charge on Cu_1–N_2 sites during the propylene epoxidation with O_2. Orange: Cu atoms, blue: N atoms, grey: C atoms, white: H atoms and red: O atoms.

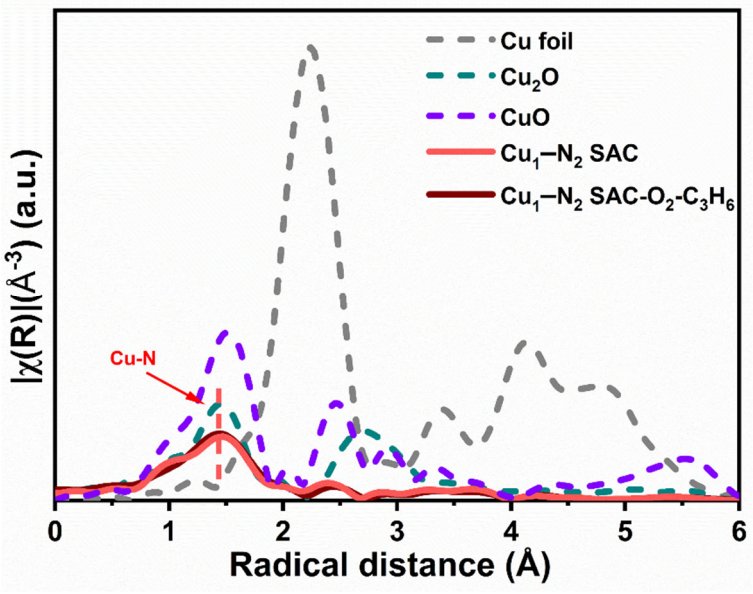

Supplementary Figure 28 | Structural characterizations. Cu *K*-edge EXAFS of Cu foil, Cu_2O, CuO, Cu_1–N_2 SAC and Cu_1–N_2 SAC-O_2-C_3H_6.

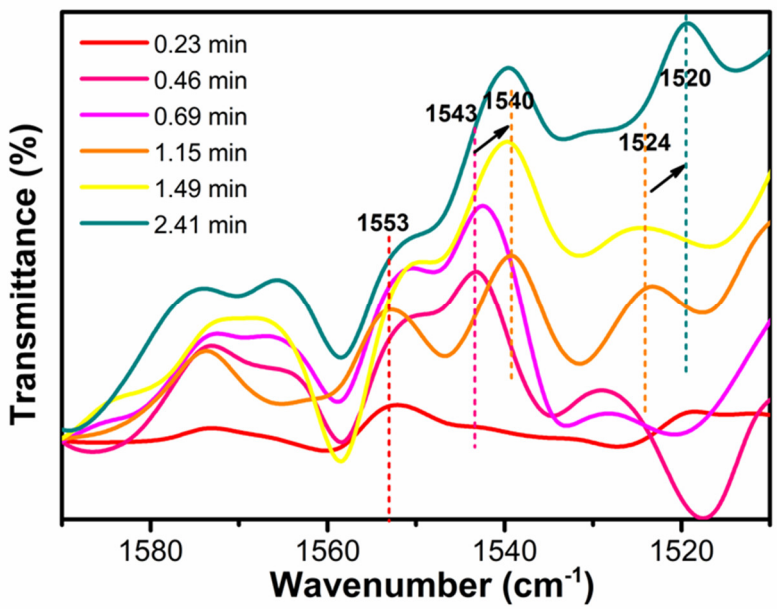

Supplementary Figure 29 | *In situ* DRIFTS spectra. *In situ* DRIFTS spectra over Cu_1–N_2 SAC at 275 °C were recorded after the PO adsorption at different times.

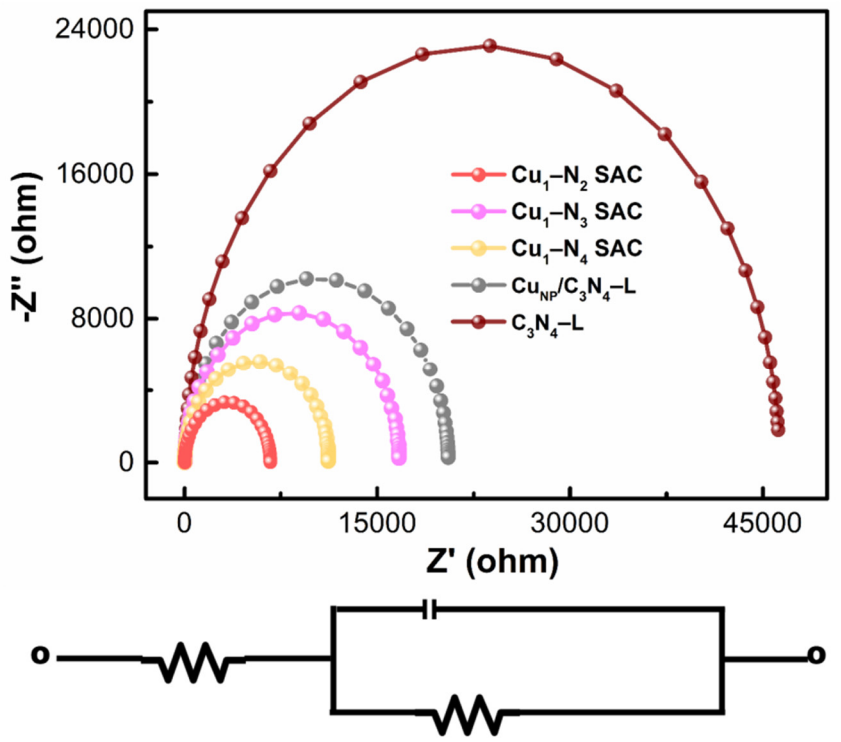

Supplementary Figure 30 | Characterization of various catalysts. EIS spectra of Cu_1–N_2 SAC, Cu_1–N_3 SAC, Cu_1–N_4 SAC, Cu_{NP}/C_3N_4–L and C_3N_4–L using a 1 M KOH electrolyte dissolved in deionized water.

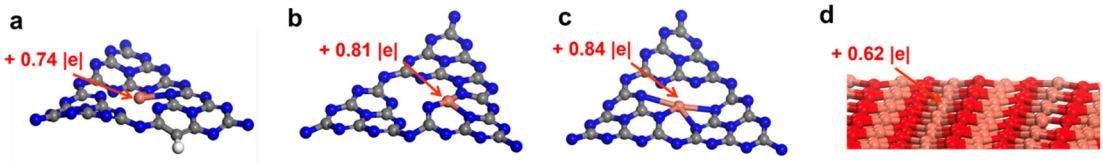

Supplementary Figure 31 | DFT analysis. Bader charge analysis for **(a)** Cu_1–N_2, **(b)** Cu_1–N_3, **(c)** Cu_1–N_4 SACs and **(d)** Cu_2O (110). Orange: Cu atoms, blue: N atoms, grey: C atoms, white: H atoms and red: O atoms.

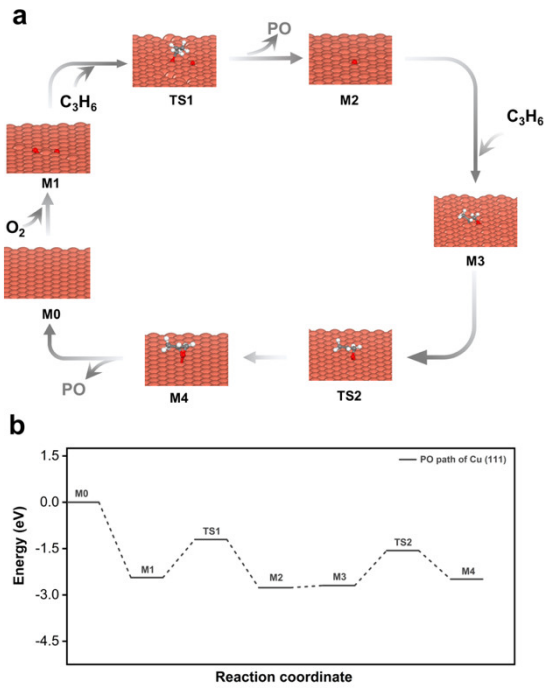

Supplementary Figure 32 | Reaction mechanism of propylene epoxidation with O_2 over Cu(111). (a) Proposed reaction pathways of the reaction of propylene epoxidation with O_2 and **(b)** Potential energy profiles PO formation. Orange: Cu atoms, grey: C atoms, white: H atoms and red: O atoms.

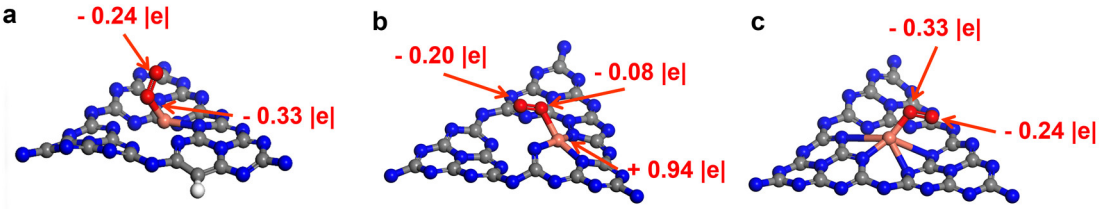

Supplementary Figure 33 | Bader charge analysis. Charge of O_2^- species on **(a)** Cu_1–N_2, **(b)** Cu_1–N_3 and **(c)** Cu_1–N_4 SACs. Orange: Cu atoms, blue: N atoms, grey: C atoms, white: H atoms and red: O atoms.

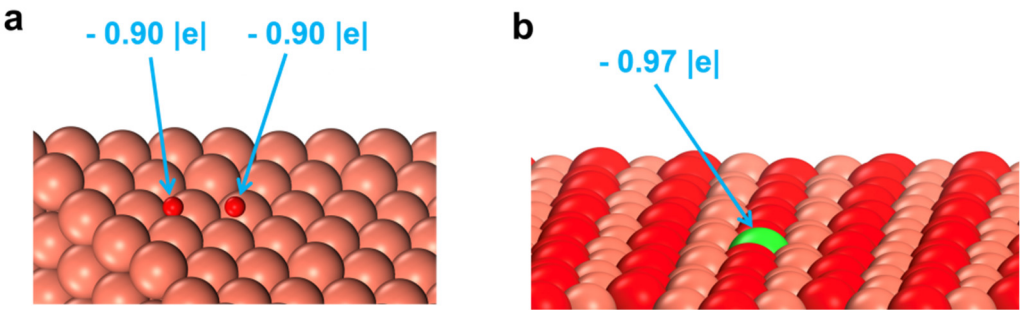

Supplementary Figure 34 | Bader charge analysis . Charge of active oxygen species on **(a)** Cu (111) and **(b)** Cu_2O (110). Orange: Cu atoms and red: O atoms.

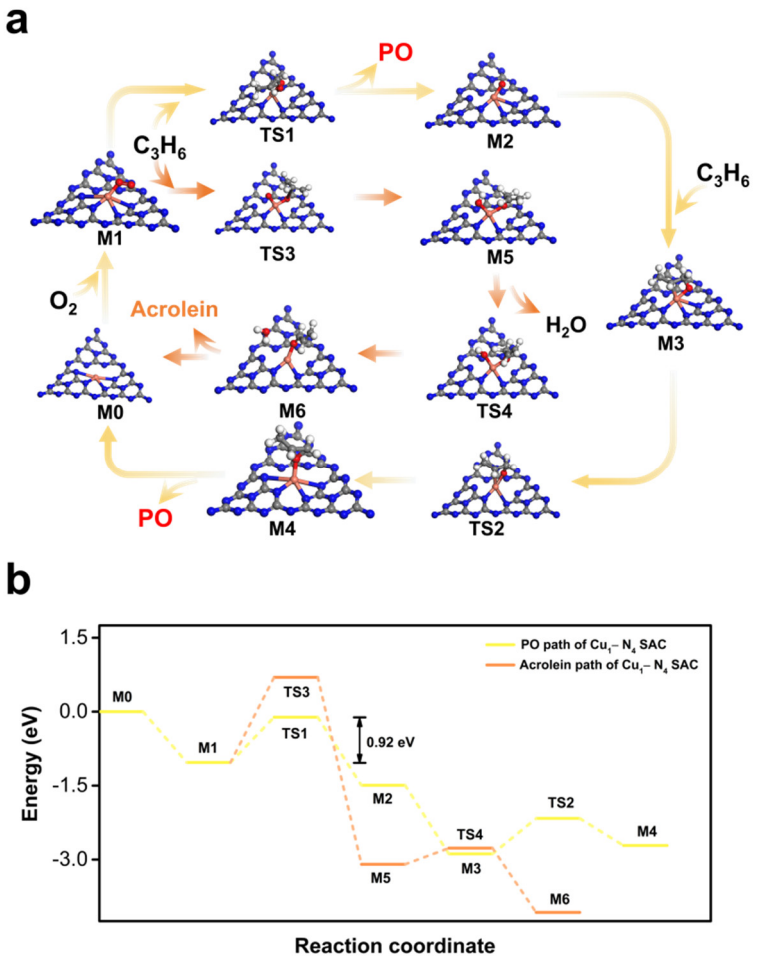

Supplementary Figure 35 | Reaction mechanism for the DEP reaction. Proposed reaction networks for propylene oxidation with O_2 over Cu_1–N_4 SAC(**a**) and corresponding energy profiles (**b**) The orange, blue, grey, red and white balls represent as Cu, N, C, O and H atoms, respectively.

Supplementary Tables

Supplementary Table 1 | Physicochemical properties of various catalysts.

Sample	Cu wt%[a]
Cu_1–N_2 SAC	23.9
Cu_1–N_3 SAC	21.9
Cu_1–N_4 SAC	24.1
Cu_{NP}/C_3N_4–L	19.6

[a] The compositions were determined by ICP-OES measurement.

Supplementary Table 2 | Carbon and nitrogen bonding compositions of various samples based on XPS analysis.

Sample	C 1*s* (%)	N 1*s* (%)			
		C−N=C	$C-NH_x$	$N-(C)_3$	Cu−N
C_3N_4	49.30	71.92	7.69	20.39	0
Cu_1–N_2 SAC	52.92	59.62	8.04	19.51	12.83
Cu_1–N_3 SAC	46.31	58.96	7.65	17.50	15.89
Cu_1–N_4 SAC	62.63	57.39	6.67	15.56	20.38

Supplementary Table 3 | EXAFS fitting data of various catalysts.

Sample	Shell	N	R (Å)	σ^2 ($Å^2$)	ΔE_0 (eV)	R factor
Cu_1–N_2 SAC	Cu–N	1.8	1.92	0.0063 ± 0.0016	4.7	0.005
Cu_1–N_3 SAC	Cu–N	2.8	1.91	0.0080 ± 0.0040	4.8	0.003
Cu_1–N_4 SAC	Cu–N	3.7	2.35	0.0107 ± 0.0046	4.6	0.015
Cu_1–N_2 SAC-O_2-C_3H_6	Cu–N	1.9	1.91	0.0067 ± 0.0044	4.6	0.008

N, coordination number; R, distance between absorber and backscatter atoms; σ^2, DebyeWaller factor to account for thermal and structural disorders; ΔE_0, threshold Energy Correction; R factor indicates the goodness of the fit.

Supplementary Table 4 | Textural properties of C_3N_4, C_3N_4–L, Cu_1–N_2 SAC, Cu_1–N_3 SAC, Cu_1–N_4 SAC and Cu_{NP}/C_3N_4–L.

Sample	S_{BET}[a] ($m^2\ g^{-1}$)	V_{mic}[b] ($cm^3\ g^{-1}$)	V_{meso}[c] ($cm^3\ g^{-1}$)
C_3N_4	1.78	0.0008	0.0069
C_3N_4–L	11.74	0.0007	0.0307
Cu_1–N_2 SAC	21.92	0.0009	0.0395
Cu_1–N_3 SAC	11.66	0.0009	0.0296
Cu_1–N_4 SAC	17.09	0.0020	0.1151
Cu_{NP}/C_3N_4–L	3.44	0.0002	0.0176

[a] BET surface area; [b] t-Plot micropore volume; [c] BJH adsorption volume.

Supplementary Table 5 | Assignment of IR bands observed in the DRIFTS spectra.

Wavenumber (cm^{-1})	Assignment	Ref.
3320	N–H stretching-vibration	[8,9]
2950, 2982, 3100	methyl symmetrical C−H vibrations	[10–12]
2310, 2380	asymmetric stretching vibration of CO_2	[13–16]
1823	C–N stretching-vibration	[17]
1740-1700	C=O stretching-vibration	[18–20]
1635	C=C stretching-vibration	[9,12,21,22]
1590-1510	C--O stretching-vibration	[10,21,23,24]
1441	CH_2 bending-vibration	[11,12]
1340-1300, 1260-1230	C–O–C asymmetric stretching	[21,23,25,26]
1288	CH bending-vibration	[14,15]
1265	Deformation-vibration of methyl groups	[21]
1210-1180	C–O stretching-vibrations	[18,19]
1123	interaction of O_2 with Cu^+ ions	[27,28]

Supplementary Table 6 | Comparison between $Cu_1–N_2$ SAC, $Cu_1–N_3$ SAC, $Cu_1–N_4$ SAC, Cu_{NP}/C_3N_4–L and other reported IB group metal catalysts for propylene epoxidation with O_2.

Catalyst	Conv. (%)	PO select. (%)	PO formation rate (mmol g_{cat}^{-1} h^{-1})	Mass (mg)	Temp. (^oC)	Flow rate (mL min^{-1})	Pressure (MPa)	Ref.
Cubic Cu_2O	0.80	10	/	200	225	50.0	0.1	15
Octahedral Cu_2O	0.67	3	/	200	200	50.0	0.1	15
Rhombic dodecahedra Cu_2O	0.8	13	0.057	200	250	50.0	0.1	15
Rhombic dodecahedra	1.0	63	0.5	200	200	50.0	0.1	11
Cl-Cu_2O	0.05	95	0.04	200	150	50.0	0.1	11
Cu/SiO_2	0.25	53	0.014	100	225	50.0	0.1	29
K^+-1% CuO_x/SBA-15	2.1	21	2.1	200	350	60.0	0.1	30
K^+-5% CuO_x/SiO_2	2.0	25	2.0	200	250	60.0	0.1	31
KAc-Cu/SiO_2	1.3	61	/	0.2 mL	275	100.0	0.1	32
Cu_7Ce	0.68	95	0.078	500	80	50.0	0.1	33
$VCe_{0.5}Cu_{0.5}$-NaCl	0.26	33	0.165	200	250	60.0	0.1	34
Au/TS-1-KOH	0.88	52	0.19	300	200	20.0	0.1	35
Ag-$CaCO_3$-NaCl	3.7	45	1.24	500	260	30.0	0.3	36
Ag-MoO_3/ZrO_2	0.6	58	0.236	0.5 mL	350	62.5	0.1	37
Ag/Y_2O_3-K_2O/α-Al_2O_3	4	47	0.303	0.5 mL	245	16.7	0.1	38
$LaMn_{0.5}Cu_{0.5}O_3$	0.02	74	0.239	200	150	30.0	0.1	39
c-Cu_2O-27	/	80	/	200	90	50.0	0.1	14
	/	70	/	200	110	50.0	0.1	14
Cu_{NP}/C_3N_4–L	1.6	8	0.163	50	325	30.0	0.1	This work
$Cu_1–N_4$ SAC	5.5	44	3.023	50	300	30.0	0.1	This work
$Cu_1–N_3$ SAC	0.4	/	/	50	350	30.0	0.1	This work
$Cu_1–N_2$ SAC	5.7	78	5.866	50	275	30.0	0.1	This work

Supplementary Table 7 | Analysis of reaction energy on $Cu_1–N_2$. Calculated barrier (E_a), reaction enthalpy (△E), and Gibbs free energy change (△G) of the key elementary steps for propylene oxidation to PO and acrolein on $Cu_1–N_2$ SAC.

Reaction step	E_a / eV	△E / eV	△G / eV
$O_2 + * \rightarrow O_2*$	-	-1.02	-0.30
$CH_3CHCH_2 + O_2* \rightarrow PO + O*$	0.76	-0.21	-0.17
$CH_3CHCH_2 + O* \rightarrow CH_3CHCH_2O*$	-	-1.36	-0.12
$CH_3CHCH_2O* \rightarrow PO*$	0.47	0.22	0.17
$CH_3CHCH_2+O_2* \rightarrow OH* + CH_2CHCH_2O*$	1.65	-2.10	-1.05
$OH* + CH_2CHCOH_2* \rightarrow H_2O + CH_2CHCHO*$	0.34	-0.83	-1.77

Supplementary Table 8 | Analysis of reaction energy on $Cu_1–N_3$. Calculated barrier (E_a), reaction enthalpy (△E), and Gibbs free energy change (△G) of the key elementary steps for propylene oxidation to PO and acrolein on $Cu_1–N_3$ SAC.

Reaction step	E_a / eV	△E / eV	△G / eV
$O_2 + * \rightarrow O_2*$	-	-0.17	0.51
$CH_3CHCH_2 + * \rightarrow CH_3CHCH_2*$	-	-0.17	0.94
$O_2* + CH_3CHCH_2 \rightarrow CH_2CH(CH_3)OO*$	-	-1.99	-0.74
$O_2 + CH_3CHCH_2* \rightarrow CH_2CH(CH_3)OO*$	-	-1.99	-1.16
$CH_2CH(CH_3)OO* \rightarrow PO + O*$	3.32	2.32	1.14
$CH_3CHCH_2 + O* \rightarrow CH_3CHCH_2O*$	-	-3.82	-2.61
$CH_3CHCH_2O* \rightarrow PO*$	2.94	1.69	1.66
$CH_3CHCH_2+O_2* \rightarrow OH* + CH_2CHCH_2O*$	2.30	-1.11	0.02
$OH* + CH_2CHCOH_2* \rightarrow H_2O + CH_2CHCHO*$	0.18	-2.07	-2.29

Supplementary Table 9 | Analysis of reaction energy on Cu_1–N_4. Calculated barrier (E_a), reaction enthalpy (△E), and Gibbs free energy change (△G) of the key elementary steps for propylene oxidation to PO and acrolein on Cu_1–N_4 SAC.

Reaction step	E_a / eV	△E / eV	△G / eV
$O_2 + * \rightarrow O_2*$	-	-1.03	-0.34
$CH_3CHCH_2 + O_2* \rightarrow PO + O*$	0.92	-0.46	-0.41
$CH_3CHCH_2 + O* \rightarrow CH_3CHCH_2O*$	-	-1.39	-0.31
$CH_3CHCH_2O* \rightarrow PO*$	0.72	0.17	0.24
$CH_3CHCH_2+O_2* \rightarrow OH* + CH_2CHCH_2O*$	1.73	-2.06	-0.83
$OH* + CH_2CHCOH_2* \rightarrow H_2O + CH_2CHCHO*$	0.33	-0.98	-1.18

Supplementary Table 10 | Analysis of reaction energy on Cu (111). Calculated barrier (E_a), reaction enthalpy (△E), and Gibbs free energy change (△G) of the key elementary steps for propylene oxidation to PO and acrolein on Cu (111).

Reaction step	E_a / eV	△E / eV	△G / eV
$O_2 + * \rightarrow 2O*$	-	-2.9	-2.00
$CH_3CHCH_2 + 2O* \rightarrow CH_3CHCH_2O* + O*$	-	-1.12	0.10
$CH_3CHCH_2O* + O* \rightarrow PO* + O*$	1.24	1.24	0.54
$CH_3CHCH_2 + O* \rightarrow CH_3CHCH_2O*$	-	0.05	1.76
$CH_3CHCH_2O* \rightarrow PO*$	0.87	0.21	0.12

Supplementary References

1. Kresse, G. et al. Efficiency of ab-initio total energy calculations for metals and semiconductors using a plane-wave basis set. *Comput. Mater. Sci.* **6**, 15–50 (1996).
2. Kresse, G. et al. Efficient iterative schemes for *ab initio* total-energy calculations using a plane-wave basis set. *Phys. Rev. B* **54**, 11169–11186 (1996).
3. Kresse, G. et al. *Ab initio* molecular dynamics for liquid metals. *Phys. Rev. B* **47**, 558–561 (1993).
4. Kresse, G. et al. *Ab initio* molecular dynamics for open-shell transition metals. *Phys. Rev. B* **48**, 13115–13118 (1993).
5. Kresse, G. et al. From ultrasoft pseudopotentials to the projector augmented-wave method. *Phys. Rev. B* **59**, 1758–1775 (1999).
6. Monkhorst, H. et al. Special points for Brillouin-zone integrations. *Phys. Rev. B* **13**, 5188–5192 (1976).
7. Henkelman, G. et al. A climbing image nudged elastic band method for finding saddle points and minimum energy paths. *J. Chem. Phys.* **113**, 9901–9904 (2000).
8. Gnanamoorthy, G. et al. New orchestrated of X-CuTiAP (en, trien, ETA and DMA) nanospheres with enhanced photocatalytic and antimicrobial activities. *J. Ind. Eng. Chem.* **110**, 503–519 (2022).
9. Zhao, R. et al. Evaluation of degradation of pigments formed during garlic discoloration in different pH. *Food Res. Int.* **140**, 109957 (2021).
10. Liang, M. et al. The propylene oxide rearrangement catalyzed by the lewis acid sites of ZSM-5 catalyst with controllable surface acidity. *Catal. Lett.* **149**, 942–949 (2019).
11. Zhan, C. et al. Critical roles of doping Cl on Cu_2O nanocrystals for direct epoxidation of propylene by molecular oxygen. *J. Am. Chem. Soc.* **142**, 14134–14141 (2020).
12. Lu, J. et al. FT-IR study on adsorption of propylene, oxygen and propylene oxide on NaCl-modified Cu/SiO_2 catalyst. *Chinese J. Catal.* **25**, 855–861 (2004).

13. Wang, W. et al. Crystal plane effect of ceria on supported copper oxide cluster catalyst for CO oxidation: importance of metal-support interaction. *ACS Catal.* **7**, 1313–1329 (2017).
14. Xiong, W. et al. Fine cubic Cu_2O nanocrystals as highly selective catalyst for propylene epoxidation with molecular oxygen. *Nat. Commun.* **12**, 5921 (2021).
15. Hua, Q. et al. Crystal-plane-controlled selectivity of Cu_2O catalysts in propylene oxidation with molecular oxygen. *Angew. Chem. Int. Ed.* **53**, 4856–4861 (2014).
16. Chen, S. et al. Probing surface structures of CeO_2, TiO_2, and Cu_2O nanocrystals with CO and CO_2 chemisorption. *J. Phys. Chem. C.* **120**, 21472–21485 (2016).
17. Cohen, A. D. et al. Time-resolved IR detection and study of an iminooxirane intermediate. *Org. Lett.* **6**, 401–403 (2004).
18. Amenabar, I. et al. Hyperspectral infrared nanoimaging of organic samples based on Fourier transform infrared nanospectroscopy. *Nat. Commun.* **8**, 14402 (2017).
19. Kang, J. et al. Effect of amino acid-derived nitrogen and/or sulfur doping on the visible-light-driven antimicrobial activity of carbon quantum dots: A comparative study. *Chem. Eng. J.* **420**, 129990 (2021).
20. He, X. et al. In situ infrared nanospectroscopy of the local processes at the Li/polymer electrolyte interface. *Nat. Commun.* **13**, 1398 (2022).
21. Wang, Y. et al. Study on the reaction mechanism of the propylene oxide rearrangement via in situ DRIFTS. *Chem. Eng. J.* **307**, 1047–1054 (2017).
22. Chinnathambi, A. et al. Biosynthesis of TiO_2 nanoparticles by Acalypha indica; photocatalytic degradation of methylene blue. *Appl. Nanosci.* (2021) doi:10.1007/s13204-021-01761-3.
23. Li, W. et al. Direct propylene epoxidation with molecular oxygen over cobalt-containing zeolites. *J. Am. Chem. Soc.* **144**, 4260–4268 (2022).
24. Zhang, B. et al. Zn modification of Beta zeolite: Effect on acid sites and propylene oxide rearrangement. *Chem. Phy.* **539**, 110983 (2020).
25. Zhang, Q. et al. Direct insights into the role of epoxy groups on cobalt sites for acidic H_2O_2 production. *Nat. Commun.* **11**, 4181 (2020).

26. Acik, M. et al. Unusual infrared-absorption mechanism in thermally reduced graphene oxide. *Nat. Mater.* **9**, 840–845 (2010).
27. Zhang, Y. et al. NH_3 sensing mechanism investigation of CuBr: Different complex interactions of the Cu^+ ion with NH_3 and O_2 molecules. *J. Phys. Chem. C* **115**, 2014–2019 (2011).
28. Liu, N. et al. Bottom-up synthesis of two-dimensional composite via CuBDC-ns growth on multilayered MoS_2 to boost CO_2 permeability and selectivity in Pebax-based mixed matrix membranes. *Sep. Purif. Technol.* **282**, 120007 (2022).
29. Vaughan, O. et al. Copper as a selective catalyst for the epoxidation of propene. *J. Catal.* **236**, 401–404 (2005).
30. Chu, H. et al. Copper-catalyzed propylene epoxidation by molecular oxygen: Superior catalytic performances of halogen-free K^+-modified CuO_x/SBA-15. *J. Catal.* **241**, 225–228 (2006).
31. Zhu, W. et al. Cu(I)-catalyzed epoxidation of propylene by molecular oxygen. *J. Phys. Chem. C* **112**, 7731–7734 (2008).
32. Su, W. et al. A molecular insight into propylene epoxidation on Cu/SiO_2 catalysts using O_2 as oxidant. *J. Catal.* **268**, 165–174 (2009).
33. Baidya, T. et al. Low-temperature propylene epoxidation activity of CuO–CeO_2 catalyst with CO + O_2: role of metal-support interaction on the reducibility and catalytic property of CuO_x species. *J. Phys. Chem. C* **124**, 14131–14146 (2020).
34. Lu, J. et al. Epoxidation of propylene on NaCl-modified $VCe_{1-x}Cu_x$ oxide catalysts with direct molecular oxygen as the oxidant. *J. Catal.* **211**, 552–555 (2002).
35. Huang, J. et al. Propene epoxidation with dioxygen catalyzed by gold clusters. *Angew. Chem. Int. Ed.* **48**, 7862–7866 (2009).
36. Lu, J. et al. Direct propylene epoxidation over modified Ag/$CaCO_3$ catalysts. *Appl. Catal. A-Gen.* **302**, 283–295 (2006).
37. Jin, G. et al. Effect of preparation condition on performance of Ag–MoO_3/ZrO_2 catalyst for direct epoxidation of propylene by molecular oxygen. *J. Mol. Catal. A-Chem.* **232**, 165–172 (2005).

38. Yao, W. et al. Epoxidation of propylene by molecular oxygen over the Ag–Y_2O_3–K_2O/α–Al_2O_3 Catalyst. *Catal. Lett.* **119**, 185–190 (2007).
39. Zhang, X. et al. Activation of molecular oxygen over Mn-doped La_2CuO_4 perovskite for direct epoxidation of propylene. *Catal. Sci. Technol.* **12**, 2426–2437 (2022).